AIAA JOURNAL
Vol. 48, No. 3, March 2010

Nearly All-Speed, Stabilized Time-Accurate Upwind Scheme on Unstructured Grid

Ching Y. Loh* and Philip C. E. Jorgenson†
NASA John H. Glenn Research Center at Lewis Field, Cleveland, Ohio 44135

DOI: 10.2514/1.43453

A time-accurate, upwind, finite volume method for computing compressible flows on unstructured grids is presented. The method is second-order-accurate in space and time and yields high resolution in the presence of discontinuities. In the basic Euler and Navier–Stokes upwind scheme, many concepts of high-order upwind schemes are adopted: the surface flux integrals are carefully treated, a Cauchy–Kowalewski time-stepping scheme is used in the time-marching stage, and a multidimensional limiter is applied in the reconstruction stage. However, even with these up-to-date improvements, the basic upwind scheme is still plagued by the so-called pathological behaviors (for example, the carbuncle, the expansion shock, etc.), which are mostly triggered due to some undesirable local numerical instability. A simple multidimensional dissipation model is used to systematically suppress such behaviors and stabilize the scheme for flows at high Mach numbers, whereas for flows at very low Mach number (for example, $M = 0.02$), it is found that computation can be directly carried out without invoking preconditioning. The modified, stabilized scheme is referred to as the enhanced time-accurate upwind scheme (Loh, C. Y., and Jorgenson, P. C. E., "A Time Accurate Upwind Unstructured Finite Volume Method for Compressible Flow with Cure of Pathological Behaviors," AIAA Paper 2007-4463, 2007.) in this paper. The unstructured grid capability renders flexibility for use in complex geometry, and the present enhanced time-accurate upwind Euler and Navier–Stokes scheme is capable of handling a broad spectrum of flow regimes from high supersonic to subsonic at very low Mach number, appropriate for both computational fluid dynamics and computational aeroacoustics. Numerous examples are included to demonstrate the robustness of the scheme.

Nomenclature

E_3	=	space-time Euclidean space
e	=	internal energy
$\mathbf{F}, \mathbf{G}, \mathbf{H}$	=	flux vectors
$\mathbf{F}_k^{n+1/2}$	=	$\mathbf{F}$ flux vector at time step $n + 1/2$ and the kth edge (surface) of the cell
h	=	enthalpy
α	=	index number for van Albada limiter
β	=	weighing factor for numerical dissipation
γ	=	ratio of specific heat
Δt	=	time step size
Δv	=	volume of grid cell
Δl_k	=	length of the kth edge of the cell
δ_0	=	acoustic wave amplitude factor
μ	=	bulk viscosity
ρ	=	density
∇	=	divergence operator

Subscripts

i, v	=	inviscid and viscous components
L or R	=	left or right state for Riemann solver
n	=	number of time step
n_x, n_y, n_z	=	components of unit normal vector at cell surface
p	=	static pressure
Re	=	Reynolds number
S	=	surface of a control volume or cell
Sr	=	Strouhal number
t	=	time
$\mathbf{U}$	=	the conservative flow variable vector
u, v, w	=	velocity components
x, y, z	=	Cartesian coordinates

Presented as Paper 4463 at the 18th AIAA Computational Fluid Dynamics Conference, Miami, FL, 25–28 June 2007; received 6 April 2009; revision received 28 September 2009; accepted for publication 13 November 2009.

*Senior Research Scientist, Taitech, Inc., Mail Stop 5-11, 21000 Brookpark Road; ching.y.loh@grc.nasa.gov. Senior Member AIAA.

†Aerospace Engineer, Mail Stop 5-11, 21000 Brookpark Road; jorgenson@nasa.gov.

I. Introduction

FINITE volume (FV) schemes are popular in computational fluid dynamics (CFD) and computational aeroacoustics (CAA) primarily due to their robustness and geometric flexibility. The FV schemes are based on the Gauss divergence theorem applied to a control volume (CV) and consist of two steps. In the first (reconstruction) step, with given initial conditions, the cell average-flow variables are reconstructed into linear or higher-order polynomials within the CV. The second (evolution) step involves computing the surface fluxes of the CV; the cell averaged values of flow variables are then obtained for a solution at the next time level. The surface flux calculation in these schemes can be categorized into two types: the centered schemes and the upwind schemes [1]. Although the upwind schemes require a Riemann solver (exact or approximate), the centered schemes, such as the NT (Nessyahu–Tadmor) [2] scheme and the conversion element/solution element (CE/SE) scheme [3,4], do not.

There are currently many popular upwind schemes being used in CFD and CAA. The Godunov scheme and the total-variation-diminishing high-resolution schemes [5,6] are considered to be the fundamental upwind schemes. In the past decades, there has been significant progress in improving the accuracy of the upwind methods by using higher-order approximations (e.g., the essentially nonoscillatory [7] and weighted essentially nonoscillatory [8] schemes, the discontinuous Galerkin [9] scheme, the spectral finite volume, and the spectral difference schemes [10,11]. However, CPU time and computer memory with these high-order schemes are also much higher.

The purpose of this paper is to present a practical method that avoids high computational costs but with reasonable accuracy while retaining its robustness [12]. We will focus on the construction of

such a time-accurate upwind FV scheme for the Euler and Navier–Stokes equations on unstructured grids (triangular or tetrahedral).

In the first step of the work, a basic upwind scheme is chosen similar to the one presented in [1] for solving the Euler equations. In the basic scheme, many concepts of high-order upwind schemes are adopted, such as careful evaluation of surface fluxes, Cauchy–Kowalewski time stepping, multidimensional limiting [3,4], etc.

As is well known, the upwind methods are prone to exhibit pathological behaviors [13–19] such as the carbuncle and the expansion shock. In nature, such behaviors are due to some local numerical instability or lack of dissipation [13–18]. For various pathological behaviors, researchers have considered different implementations of dissipation in upwind schemes (e.g., [13]). In the second step, to enhance the capabilities of the basic upwind scheme, the present work takes a systematic approach to stabilize the scheme. A multidimensional numerical dissipation model [12,18] is implemented in the basic scheme. The resulting scheme is now an enhanced time-accurate upwind (ETAU) scheme. The new ETAU scheme provides a systematic cure for these undesired behaviors with high-flow Mach numbers and is nominally second-order-accurate in space and time, yielding high resolution in the presence of discontinuities.

Furthermore, as a result of the careful, multidimensional treatments, the ETAU scheme is found capable of computing flows at very low Mach number (e.g., $M = 0.02$), without invoking preconditioning. The ETAU scheme is then rendered as a nearly all-speed or Mach-number-insensitive upwind scheme. For flows in different Mach number regimes (i.e., low, medium, and high Mach numbers), one needs only to adjust one or two parameters in the scheme to accommodate a computation.

The governing equations and the basic unstructured Euler and Navier–Stokes solver are briefly described in Sec. II. Section III is devoted to the cure of the pathological behaviors at high-flow Mach number that warrants a stable scheme: ETAU. Several examples of flows at high Mach numbers are presented in Sec. IV to demonstrate how such annoying behaviors are suppressed in a systematic way. In Secs. V and VI, the ETAU Euler and Navier–Stokes solver is tested in numerical examples from supersonic to low subsonic flow speed, with emphasis on stable, long run time viscous flows for CAA computations. Concluding remarks are addressed in Sec. VII.

II. Basic Unstructured Euler and Navier–Stokes FV Solver

Because computer time and memory still need to be considered when computing time-accurate unsteady flows, an upwind FV scheme that is second-order-accurate (in the absence of flow discontinuities) in space and time is chosen. The basic upwind scheme includes many attributes often found in the construction of high-order schemes: the geometrical quantities are calculated as accurately as possible, the use of a Cauchy–Kowalewski-type evaluation of the time derivative and a multidimensional limiter [3,4] for the reconstruction stage. A brief description of the basic upwind scheme is outlined below, beginning with the Euler and Navier–Stokes (Euler and N–S) equations in conservative form.

A. Conservation Form of the Unsteady Compressible Euler and Navier–Stokes Equations

The conservative form of the two-dimensional Euler and N–S equations are briefly sketched here. Let ρ, u, v, p, and γ be the density, the two velocity components, static pressure, and constant specific heat ratio, respectively. The two-dimensional unsteady Euler and N–S equations are written in the following standard conservative form:

$$\mathbf{U}_t + \mathbf{F}_x + \mathbf{G}_y = \mathbf{0} \tag{1}$$

where x, y, and t are the streamwise, transverse, and time coordinates, respectively. The flux vectors are further split into inviscid and viscous fluxes:

$$\mathbf{F} = \mathbf{F}_i - \mathbf{F}_v, \qquad \mathbf{G} = \mathbf{G}_i - \mathbf{G}_v$$

The conservative flow variable vector $\mathbf{U}$ and the inviscid flux vectors $\mathbf{F}_i$ and $\mathbf{G}_i$ are given in nondimensional form as

$$\mathbf{U} = \begin{pmatrix} U_1 \\ U_2 \\ U_3 \\ U_4 \end{pmatrix} = \begin{pmatrix} \rho \\ \rho u \\ \rho v \\ \rho e \end{pmatrix}, \quad \mathbf{F}_i = \begin{pmatrix} \rho u \\ \rho u^2 + p \\ \rho uv \\ \rho uH \end{pmatrix}, \quad \mathbf{G}_i = \begin{pmatrix} \rho v \\ \rho uv \\ \rho v^2 + p \\ \rho vH \end{pmatrix}$$

Here, the (total) energy has the form

$$e = \frac{p}{\rho(\gamma - 1)} + \frac{1}{2}(u^2 + v^2)$$

and the enthalpy is $H = p/\rho + e$. The nondimensionalized viscous flux vectors $\mathbf{F}_v$ and $\mathbf{G}_v$ are written in conservation form [20] as

$$\mathbf{F}_v = \begin{pmatrix} 0 \\ \mu(2u_x - \frac{2}{3}\nabla\cdot\mathbf{V}) \\ \mu(v_x + u_y) \\ \mu\left[2uu_x + (u_y + v_x)v - \frac{2}{3}(\nabla\cdot\mathbf{V})u + \frac{\gamma}{Pr}\frac{\partial}{\partial x}\left(\frac{U_4}{U_1} - \frac{u^2+v^2}{2}\right)\right] \end{pmatrix}$$

and

$$\mathbf{G}_v = \begin{pmatrix} 0 \\ \mu(v_x + u_y) \\ \mu(2v_y - \frac{2}{3}\nabla\cdot\mathbf{V}) \\ \mu\left[2vv_y + (u_y + v_x)u - \frac{2}{3}(\nabla\cdot\mathbf{V})v + \frac{\gamma}{Pr}\frac{\partial}{\partial y}\left(\frac{U_4}{U_1} - \frac{u^2+v^2}{2}\right)\right] \end{pmatrix}$$

where u_x, u_y, v_x, and v_y are the flow velocity gradients with Pr being the Prandtl number; $\mu = 1/Re$ is the dynamic viscosity where Re is the Reynolds number; and the velocity divergence is $\nabla\cdot\mathbf{V} = u_x + v_y$. For air at standard conditions, $Pr = 0.72$ and $\gamma = 1.4$.

B. Cell Surface Flux Evaluation and the Time-Marching (Evolution) Stage

A typical two-dimensional unstructured triangular cell used in the scheme is illustrated in Fig. 1. Here, ΔABC is a triangular cell centered at O; D, E, and F are the centers of the neighboring triangular cells. The flow variables at the previous time step are stored at these cell centers. By considering (x, y, t) as coordinates of a three-dimensional Euclidean space E_3 and using the Gauss divergence theorem, it follows that Eq. (1) is equivalent to the integral conservation law:

$$\oint_S \mathbf{I}_m \cdot d\mathbf{s} = \mathbf{0}, \qquad m = 1, 2, 3, 4, \tag{2}$$

where S denotes the surface around a space-time CV in E_3 (e.g., the prism ABC–$A'B'C'$ in Fig. 1b) and $\mathbf{I}_m = (\mathbf{F}_m, \mathbf{G}_m, \mathbf{U}_m)$. For the surface integrals in Eq. (2), following the concepts of high-order upwind schemes [10,11,21], Gaussian quadratures are required. Here, for second-order accuracy, the only Gaussian point is the

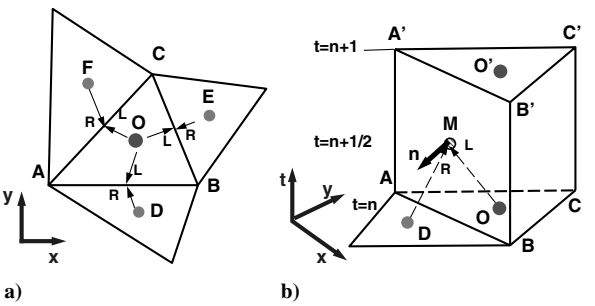

Fig. 1 Sketch of a) a typical unstructured triangular grid in two-dimensional space and b) control volume in E_3.

centroid of each space-time hyper surface (e.g., M in Fig. 1b) and the integrands are approximated by linear functions. Details are as follows.

The inviscid part of the fluxes $\mathbf{F}_k^{n+1/2}$ and $\mathbf{G}_k^{n+1/2}$ are generated via a Riemann solver (RS) (e.g., Roe's RS [22]). At time level $t = n\Delta t$, $\mathbf{U}^n$ is given at all triangular cell centers (e.g., O, D, E, and F in Fig. 1a). The spatial gradients $\mathbf{U}_x$ and $\mathbf{U}_y$ can then be reconstructed via a multidimensional limiter as described below. The left and right (L and R in Fig. 1a) states at the center of each surface of the space-time CV are established by linear Taylor expansion from their corresponding cell centers. For instance, at the center, M, of the surface $ABB'A'$ (see Fig. 1b), the R and L states are, respectively,

$$\mathbf{U}_R^{n+1/2} = \mathbf{U}_D^n + (\mathbf{U}_x^n)_D \Delta x + (\mathbf{U}_y^n)_D \Delta y + (\mathbf{U}_t^n)_D \frac{\Delta t}{2} \tag{3}$$

$$\mathbf{U}_L^{n+1/2} = \mathbf{U}_O^n + (\mathbf{U}_x^n)_O \Delta x + (\mathbf{U}_y^n)_O \Delta y + (\mathbf{U}_t^n)_O \frac{\Delta t}{2} \tag{4}$$

Here, the subscripts O and D indicate which cell center flow variables are used, and Δx and Δy correspond to either DM or OM. Note that because the outgoing unit normal is chosen, the R state always comes from the neighboring cell centers (D, E, or F). Evaluations of the time derivatives $\mathbf{U}_t^n$and spatial gradients $\mathbf{U}_x^n$ and $\mathbf{U}_y^n$are described, respectively, in Secs. II.C and II.D. This procedure with inviscid fluxes was outlined by Huynh [1] for solving the Euler equations. The evaluation of the viscous fluxes $\mathbf{F}_v^{n+1/2}$ and $\mathbf{G}_v^{n+1/2}$ follows the formulations in Sec. II.A, but only the R-state data are used. As the flow variables are assumed linear within each cell, spatial derivatives (gradients) are constant therein and can be applied directly without using Taylor expansion.

The simple quadrature of the surface integrals in Eq. (2) leads to the update formulation of $\mathbf{U}$ at O from time step n to $n + 1$:

$$\mathbf{U}^{n+1} = \mathbf{U}^n - \frac{\Delta t}{\Delta s} \sum_{k=1}^{3} [\mathbf{F}_k^{n+1/2}(n_x)_k + \mathbf{G}_k^{n+1/2}(n_y)_k] \Delta l_k \tag{5}$$

where $\mathbf{F}_k$, $\mathbf{G}_k$, $(n_x)_k$, and $(n_y)_k$ ($k = 1$, 2, and 3) are, respectively, the two flux vectors, the outgoing unit normal vector components at the centers of the three cylindrical surfaces $ABB'A'$, $BCC'B'$, and $CAA'C'$. The lengths of the edges of the triangular cell ΔABC, AB, BC, and CA are represented by Δl_k ($k = 1$, 2, and 3); Δs the area of ΔABC and Δt the time step size.

With the introduction of a multidimensional dissipation model (Sec. III.C), the basic scheme (5) will be augmented later to cure the undesired pathological behaviors and upgraded to the ETAU scheme.

C. Cauchy–Kowalewski and Lax–Wendroff Time Stepping

The Cauchy–Kowalewski concept makes use of the governing equations to represent the time derivative by the spatial derivatives. Lax and Wendroff were the first to apply the concept to the Euler equations in their well-known Lax–Wendroff scheme. The idea was followed by other researchers (e.g., the NT and CE/SE schemes [2,4]). Here, assuming all the spatial gradients $\mathbf{U}_x^n$ and $\mathbf{U}_y^n$ are already given, evaluation of $\mathbf{U}_t$ follows the Lax–Wendroff procedure:

$$\mathbf{U}_t^n = -\mathbf{F}_x^n - \mathbf{G}_y^n \tag{6}$$

As the Reynolds number Re is usually high (or viscosity μ is small), $\mathbf{F}$ and $\mathbf{G}$ can be well approximated by their inviscid portions: Eq. (6) is simplified to

$$\mathbf{U}_t^n = -\left(\frac{\partial \mathbf{F}_i}{\partial \mathbf{U}}\right)^n \mathbf{U}_x^n - \left(\frac{\partial \mathbf{G}_i}{\partial \mathbf{U}}\right)^n \mathbf{U}_y^n \tag{7}$$

$\mathbf{U}_t^n$ is then substituted, respectively, to Eq. (3) or Eq. (4) to provide R and L states for the local Riemann solver. A numerical flux for a given face is thus evaluated. Once the flux data are computed at all the cell surface, the averaged solution is updated to the $(n + 1)\Delta t$ time level (the top face of the CV, $\Delta A'B'C'$) using Eq. (5).

D. Multidimensional Limiting and the Reconstruction Stage

In the reconstruction stage, the averaged flow data $\mathbf{U}$ (i.e., $\mathbf{U}^{n+1}$) just updated at the current cell center O and at its three neighboring cell centers D, E, and F (see Fig. 1a) are used to construct a new set of spatial gradients. In general, the reconstruction process requires solving an overdetermined system (see, for example, [21]). For second-order accuracy, $\mathbf{U}$ must be reconstructed into a linear vector function within the current cell via a limiter.

Here, a multidimensional as opposed to dimension-by-dimension limiter is employed. Let u denote a component of $\mathbf{U}$; by simple finite difference, three linear equations for the gradients (u_x, u_y) are obtained:

$$(x_D - x_O)u_x + (y_D - y_O)u_y = u_D - u_O$$
$$(x_E - x_O)u_x + (y_E - y_O)u_y = u_E - u_O$$
$$(x_F - x_O)u_x + (y_F - y_O)u_y = u_F - u_O$$

Here, the subscripts O and D, E, and F denote the corresponding cell centers. Generally, any combination of two of these equations yields a set of spatial gradients for u. There are three sets of such gradients: namely, (u_x^i, u_y^i) ($i = 1$, 2, and 3). Their moduli or l_2 norms,

$$m_i = \sqrt{(u_x^{(i)})^2 + (u_y^{(i)})^2}$$

($i = 1$, 2, and 3) are calculated as a measure for later usage. Then, a multidimensional limiter based on the magnitude of the norms is applied to all spatial gradients to achieve a single, unified set of gradients for $\mathbf{U}$. Two such multidimensional limiters are recommended here: the minmod limiter and the extended van Albada limiter (weighted averaging) [23].

When the minmod limiter is employed, the gradient $(u_x^{(i)}, u_y^{(i)})$ corresponding to $m_i = \min(m_1, m_2, m_3)$ is chosen. When the extended van Albada limiter is used, let $w_1 = (m_2 m_3)^\alpha$, $w_2 = (m_1 m_3)^\alpha$, $w_3 = (m_1 m_2)^\alpha$, and $\alpha \geq 0$; the final gradients are evaluated through weighted averaging:

$$u_x = \frac{w_1 u_x^{(1)} + w_2 u_x^{(2)} + w_3 u_x^{(3)}}{w_1 + w_2 + w_3}, \qquad u_y = \frac{w_1 u_y^{(1)} + w_2 u_y^{(2)} + w_3 u_y^{(3)}}{w_1 + w_2 + w_3}$$

The extended van Albada limiter or weighted averaging was previously used in the CE/SE method [3,4]. Different α provide numerical dissipation at different levels. A small α (e.g., $\alpha = 0.5$) usually yields less dissipation. In the presence of a shock or a contact discontinuity, a larger $\alpha(=2.0)$ is needed. In the rare extreme situation with high Mach number and strong shocks, the computed gradients u_x and u_y need to be further limited by a factor in order to keep the numerical procedure stable (see, for example, [24]).

E. Extension to Three-Dimensional Space

The basic Euler and N–S upwind scheme can be consistently extended to three-dimensional space. The governing formulation equation. (1) is

$$\mathbf{U}_t + \mathbf{F}_x + \mathbf{G}_y + \mathbf{H}_z = \mathbf{0} \tag{8}$$

Here, similar to Sec. II.A, $\mathbf{U}$, $\mathbf{F}$, $\mathbf{G}$, and $\mathbf{H}$ are the three-dimensional versions of the conservative flow variables and the flux vectors. All the numerical implementations from Secs. II.B–II.D can be extended to the three-dimensional case. The update formulation equation (5) becomes

$$\mathbf{U}^{n+1} = \mathbf{U}^n - \frac{\Delta t}{\Delta v} \sum_{k=1}^{4} [\mathbf{F}_k^{n+1/2}(n_x)_k + \mathbf{G}_k^{n+1/2}(n_y)_k + \mathbf{H}_k^{n+1/2}(n_z)_k] \Delta s_k \tag{9}$$

where Δv and Δs_k ($k = 1$, 2, 3, and 4) represent the volume and the surface areas of the current tetrahedral cell.

III. Cure of the Pathological Behaviors and the Stabilized ETAU Scheme

The basic scheme described above is an improved upwind scheme of the Godunov type. The scheme works well with many benchmark-type problems but still suffers from the general symptom of the so-called pathological behaviors described by Quirk [13] and Kitamura et al. [19]. The pathological behaviors and their cure or the stabilization of the basic scheme are reviewed and discussed in this section.

A. Pathological Behaviors and How They Occur

Despite the great success of the upwind schemes, there are still some cases of failure reported by researchers: for example, the carbuncle phenomenon in the bow shock of a blunt body, the expansion shock when a supersonic flow of high Mach number passes over a sharp edge, and the kinked Mach stem when a supersonic flow passes a wedged wall, etc., [14–17,19]. It is generally agreed that insufficient dissipation and the consequent local numerical instability lead to such failures [13,14,16,18].

In the literature, for the Godunov-type upwind schemes, a general cure is switching to different Riemann solvers to gain some more dissipation. For example, an expansion shock can be cured by switching from a Roe approximate Riemann solver to an Harten–Lax–van Leer–Einfeldt (HLLE) Riemann solver [13]. A comparison of the performances of various Riemann solvers or flux-splitting is given in [14]. Lin [15] provides a way to add dissipation to flux difference splitting schemes to treat the carbuncle phenomena and the slow-moving shock instability. Other curing measures may be found in the references of these papers.

Recently, based on the previous works of these researchers, the present authors proposed a new multidimensional dissipation model to systematically cure the pathological behaviors and stabilize the upwind scheme [12,18]. For completeness, the multidimensional dissipation model is briefly reviewed and sketched below, with its implementation to the basic scheme.

In his investigation, Xu [16,17] argued that for a Godunov-type upwind scheme, the dissipation required by the numerical stability mainly comes from the Riemann solver at the cell interface. With the given L and R states across the cell interface (L and R in Fig. 2a), the Riemann solver attempts to compromise the two different states to an intermediate state for the flux by some kind of averaging. For example, in the Roe approximate Riemann solver, $\rho_L/(\rho_L + \sqrt{\rho_L \rho_R})$ is used as the weighing factor in the weighted averaging for the flow variables. The averaging process is accompanied by an entropy increase and numerical dissipation is generated. The amount of dissipation varies subject to the L and R states and is in the normal direction of the cell interface. The more they differ from each other, the more the numerical dissipation. After applying a Riemann solver to the interface between two adjacent cells, the divergence theorem stipulates that only the normal flux vector components at the interface are considered in the evaluation of surface fluxes and all the tangential components are ignored. In the tangential direction of the surface, no wave is assumed to occur and the numerical dissipation is absent.

Based on Xu's arguments, we are able to conduct a qualitative analysis to the typical pathological behaviors, such as the carbuncle. For convenience, we assume a rectangular grid, as shown in Figs. 2a and 2b, and that the grid lines AD and BC are aligned with the bow shock. For the grid cell $ABCD$ located near the stagnation point of the blunt body (see Fig. 2a), as the flow states jump sharply across BC because of the bow shock (see Fig. 2b), the RS at BC introduces numerical dissipation normal to the bow shock, but no dissipation occurs in the tangential direction. For the surface (edge) CD, as the L and R states are almost identical (e.g., $v_L = v_R$), the RS provides little or no dissipation in its normal direction or the direction aligned to the shock. Similar analysis can be applied to the other two surfaces AB and AD. Thus, the numerical solution is vulnerable to the local temporal or spatial instabilities in the direction tangent to or aligned with the shock, causing the carbuncle phenomena. Naturally, a remedy is to add some extra numerical dissipation in the tangential direction of the shock or the cell interfaces AD and BC to stabilize the numerical computation.

Another typical pathological behavior is the expansion shock that forms in supersonic flow of high Mach number past a sharp edge (see Fig. 2c). The expansion shock represents a different type of insufficient dissipation. Although the RSs at AB and BC generate numerical dissipation in the normal direction, the dissipation may not be sufficient enough, and an expansion shock appears. Quirk [13] has suggested using a more dissipative HLLE Riemann solver and smearing the expansion shock to an expansion fan. Here again, an alternative remedy is to add supplementary numerical dissipation, but this time in the direction normal to the cell interfaces AB and BC or the expansion shock.

The preceding analysis of two typical cases suggests that if there exists a dissipation model that contributes additional dissipation in both tangential and normal directions or omnidirectionally, these pathological phenomena may be cured.

A multidimensional dissipation model proposed in [12,18] is employed in the present paper, which is external to the RS, to systematically control and suppress the pathological behaviors and to stabilize the scheme. The model adds *omnidirectional* dissipation to the basic upwind scheme.

B. One-Dimensional Dissipation Model

To explain how the dissipation model works, we begin with a simple one-dimensional scalar advection equation:

$$\frac{\partial u}{\partial t} + \frac{\partial u}{\partial x} = 0 \tag{10}$$

Two simple one-dimensional finite difference schemes are reviewed. The first scheme is a scheme of forward difference in time and central difference in space:

$$u_j^{n+1} = u_j^n + 0.5r(u_{j+1}^n - u_{j-1}^n) = u_a$$

where $r = \Delta t/\Delta x$. It is well known that such a scheme is unconditional unstable. However, if u_j^n is replaced by an average of u

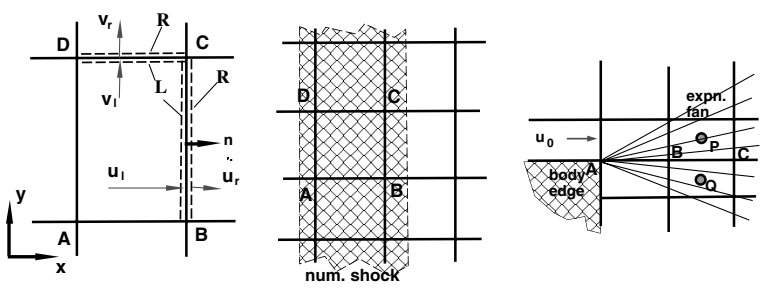

a) b) c)

Fig. 2 Grid structure associated with pathological behaviors: a) the cell *ABCD* showing the forming of dissipation in a Riemann solver: L and R correspond to left and right states and b) location of the cell relative to the shock; c) grid structure near a sharp edge in the expansion shock case: *P* and *Q* are cell centers.

at the adjacent nodes $j-1$ and $j+1$, the scheme becomes the Lax–Friedrichs scheme

$$u_j^{n+1} = 0.5(u_{j+1}^n + u_{j-1}^n) + 0.5r(u_{j+1}^n - u_{j-1}^n) = u_b$$

which is stable for $r \leq 1$. Here, we have learned that when replacing u_j by an average of u at the adjacent nodes, a certain amount of dissipation is added to the scheme, making it stable.

C. Implementation of Multidimensional Dissipation Model and the ETAU Scheme

Based on the preceding one-dimensional dissipation model, and for better performance, a slightly different multidimensional model with controllable dissipation is proposed [12,18]. Here, the process is made fully embedded in the numerical procedure at no additional cost in operation.

As shown in Fig. 3a, let ΔABC be the current cell, M, N, and P be, respectively, the midpoints of its edges AB, BC, and CA (i.e., cell surface centers). Note that the triangle ΔMNP is also centered at O. The R states at these midpoints at time level n are extrapolated from their respective neighboring cell centers D, E, and F (see Fig. 1a) by Taylor expansion:

$$\mathbf{U}_M^n = \mathbf{U}_D^n + (\mathbf{U}_x^n)_D \Delta x + (\mathbf{U}_y^n)_D \Delta y$$
$$\mathbf{U}_N^n = \mathbf{U}_E^n + (\mathbf{U}_x^n)_E \Delta x + (\mathbf{U}_y^n)_E \Delta y$$
$$\mathbf{U}_P^n = \mathbf{U}_F^n + (\mathbf{U}_x^n)_F \Delta x + (\mathbf{U}_y^n)_F \Delta y$$

They are an intermediate step of Eq. (3) and cost no extra CPU time in computation. The average of these pointwise values

$$\tilde{\mathbf{U}} = (\mathbf{U}_M^n + \mathbf{U}_N^n + \mathbf{U}_P^n)/3$$

is an approximation of $\mathbf{U}_O$ with spatial smearing. Then, $\mathbf{U}^n$ in Eq. (5) is replaced by a weighted average of $\mathbf{U}^n$ and $\tilde{\mathbf{U}}$ [i.e., Eq. (5)] becomes

$$\mathbf{U}^{n+1} = \beta\tilde{\mathbf{U}} + (1-\beta)\mathbf{U}^n - \frac{\Delta t}{\Delta s}\sum_{k=1}^{3}[\mathbf{F}_k^{n+1/2}(n_x)_k + \mathbf{G}_k^{n+1/2}(n_y)_k]\Delta l_k \tag{11}$$

Here, β and $0 \leq \beta < 1$ is the weighing factor, which controls the numerical dissipation. By this weighted averaging process, some numerical dissipation is introduced to the scheme. For most cases, the flow is insensitive to the value of β and setting $\beta = 10^{-4} - 10^{-3}$ is appropriate. Sometimes, even $\beta = 0$ works fine. For flows with extremely high Mach number and strong shocks, particularly in the presence of the pathological behaviors, β may need to be increased up to the level of 10^{-1}. To avoid excessive dissipation, one should keep β as low as possible. One could even have the option to choose different βs in different flow regions.

With the dissipation model added to the basic scheme, it is referred to the ETAU scheme. The scheme in Eq. (11) falls within the class of second-order-accurate upwind schemes. For general unstructured grids, when the flow is continuous around the cell (ΔABC in Fig. 1a), $\tilde{\mathbf{U}} = \mathbf{U}^n + O(h^2)$, where h is the average grid size. The ETAU scheme in Eq. (11) is hence still spatially second-order-accurate.

Equation (11) can be consistently extended to a three-dimensional scheme with tetrahedral grid cells (see Fig. 3b). Further discussion on the accuracy of upwind finite volume schemes using arbitrary unstructured polyhedral grids for three-dimensional flows can be found in [21].

In the following sections, numerical examples with high, medium, and low Mach numbers are displayed, including the cure of pathological behaviors.

IV. Numerical Examples for High-Mach-Number Flows with Pathological Behaviors

In this section, we demonstrate how several well-known pathological behaviors are systematically suppressed with the ETAU scheme simply by turning on and adjusting β.

A. Expansion Shock

Consider the problem of a strong shock diffracting over a 90 deg edge [13]. Here, the shock Mach number is $M_s = 5.09$. There are about 14,000 triangular cells in the domain. Initially, the flow is set to the quiescent ambient condition

$$(\rho_0, u_0, v_0, p_0) = (1, 0, 0, 1/\gamma), \qquad \gamma = 1.4$$

and $M_s = 5.09$ conditions are imposed at the inlet:

$$(\rho_i, u_i, v_i, p_i) = (5.0294, 4.0779, 0, 21.4710)$$

At the top, bottom, and along the surfaces of the rectangular block, the slip-wall condition is imposed. A simple extrapolation condition is applied to the outlet boundary. The van Albada index α is set at 2.0. Figure 4 illustrates the density contours with or without the cure. With β changing slightly from 0 to 0.001, the expansion shock disappears.

B. Kinked Mach Stem

Another example of the pathological behaviors is the kinked Mach stem over a ramp of 30 deg [13]. There are 36,240 triangular cells in the grid. Initially, the flow is set at the quiescent ambient condition

$$(\rho_0, u_0, v_0, p_0) = (1, 0, 0, 1/\gamma)$$

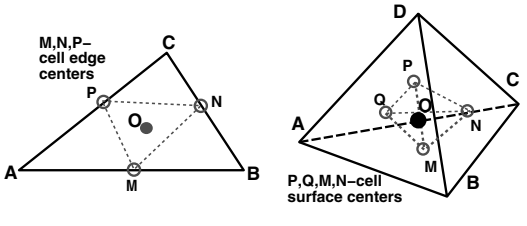

a) b)

Fig. 3 Dissipation models in two-dimensional and three-dimensional spaces: a) for two-dimensional triangular cell, O is the cell center, M, N, and P are the cell edge centers and b) for three-dimensional tetrahedral cell, O is the cell center, M, N, P, and Q are the cell surface centers.

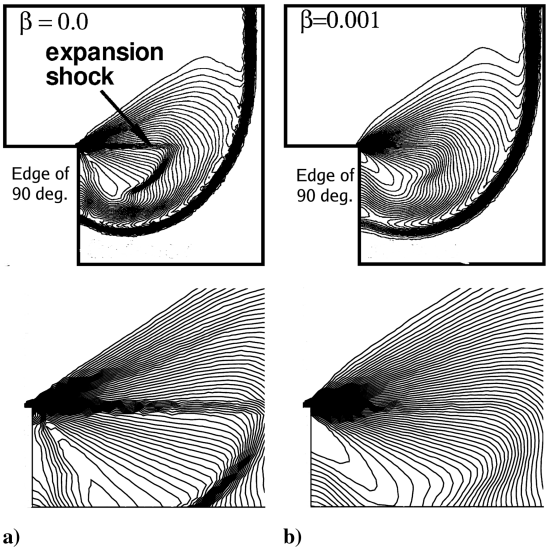

a) b)

Fig. 4 Supersonic flow diffracted over an edge of 90 deg: a) at $\beta = 0$, expansion shock is present and b) at $\beta = 0.001$, expansion shock disappears; details of the expansion shock and expansion fan are displayed at the bottom.

and $M_s = 5.5$ conditions are imposed at the inlet:

$$(\rho_i, u_i, v_i, p_i) = (5.1489, 4.4318, 0, 25.0893)$$

Boundary conditions at the top, bottom, and the ramp surface are the slip-wall conditions. Simple extrapolation is imposed at the outlet boundary. Figure 5 demonstrates how a correct Mach stem is recovered by setting $\beta = 10^{-3}$.

C. Carbuncle Phenomenon

The carbuncle phenomenon occurs with most upwind schemes when computing supersonic flow past a blunt body with a bow shock. In this example, the blunt body is a half-circular cylinder with a slip-wall boundary condition. Simple extrapolation is applied to the outflow boundaries. A freestream of $M = 10$ is imposed at the inflow boundary. For flows with shocks, the index parameter α in the van Albada limiter is usually set at 2. For high-Mach-number flows with shocks, the dissipation parameter β may need to increase from the level of 10^{-3} to 10^{-2} or even 10^{-1}. To avoid excessive damping, one should keep β as low as possible. Also for high-Mach-number flows with shocks, we note that for convergence, sometimes the spatial gradients of the (conservative) flow variables after limiting might still need to further reduce by a factor c and $0 \leq c \leq 1$ (see, for example, [24]).

As the carbuncle phenomenon is a focus of research, this problem is tested on both structured and unstructured grids. The first grid here is actually a triangulated structured grid but treated as unstructured data. There are about 80,000 triangular cells in the computational domain. As shown in Figs. 6a and 6b, the carbuncle is prominent with $\beta = 0$ but disappears when a maximum $\beta = 0.05$ is applied. Here, β is at its maximum value near the stagnation area where carbuncle phenomenon occurs and gradually tapers down to 0.01.

Recently, Kitamura et al. [19] reported that with an upwind scheme, the carbuncle depends on a variety of issues, such as the free-stream Mach number, grid shape, etc. Also, curing of the carbuncle is hard on a truly unstructured grid. Our next test is on a truly unstructured grid. There are about 75,000 triangular cells in the grid. All the flow conditions are identical to the case with a triangulated structured grid.

For the present ETAU scheme, in order to achieve a correct solution as compared to Fig. 6b, it is found necessary to adjust only the maximum β. The treatment is simple and effective. When the maximum β in the stagnation region is increased to 0.25, the carbuncle is completely suppressed. With increased dissipation, the bow shock in the stagnation region appears thicker (see Figs. 6c and 6d), which is a tradeoff for the unstructured grid (without adaptive mesh refinement techniques). Note that the triangulated grid in Figs. 6a and 6b is much coarser near the top and bottom corners and the bow shock in Figs. 6b spreads out. Also, the isobar contour lines used in Figs. 6c and 6d are thicker.

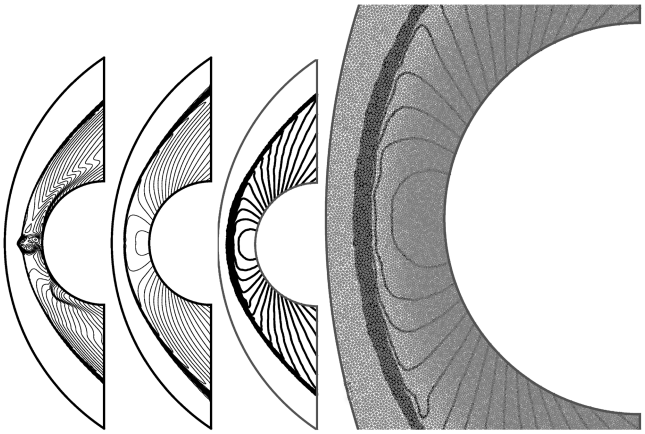

Fig. 6 Supersonic $M = 10$ flow past a circular blunt body on a triangulated structured grid: a) carbuncle with Godunov scheme ($\beta = 0$) and b) with max. $\beta = 0.05$ imposed, the carbuncle phenomenon disappears; on a truly unstructured grid: c) isobars with max $\beta = 0.25$ and d) close-up of the stagnation region with the grid.

D. Slowly Moving Shock

Here, the one-dimensional problem is computed in a two-dimensional domain. A grid consisting of 800 uniform triangular cells is used, spanning between $0 \leq x \leq 32$. Initially, a strong shock is located at $x = 15$ with the left states and the right states:

$$(\rho_l, u_l, p_l) = (3.86, 0.81, 10.34), \qquad (\rho_r, u_r, p_r) = (1, 3.44, 1)$$

These states are also imposed as the inflow and outflow boundary conditions. At the top and bottom of the domain, the usual reflective slip-wall conditions are imposed. With $\Delta t = 0.002$, after running 10,000 steps, the slow shock moves only from $x = 15$ to $x = 17$, as shown in Fig. 7. Figure 7 also shows that by increasing β from 0 to 0.3 and 0.5, the spurious oscillation is suppressed or eliminated.

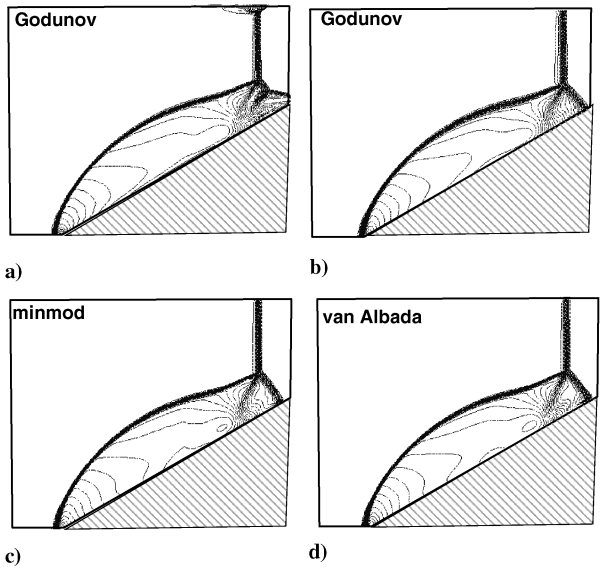

Fig. 5 Supersonic flow over a ramp with recovery of the correct Mach stem: a) Godunov scheme with no cure ($\beta = 0$): noise at the top wall and the kinked Mach stem are clearly shown; b) Godunov scheme with cure ($\beta = 0.001$): the noise disappears and a correct Mach stem is recovered; c) high resolution with minmod limiter ($\beta = 0.001$); and d) high resolution with van Albada limiter ($\beta = 0.001$).

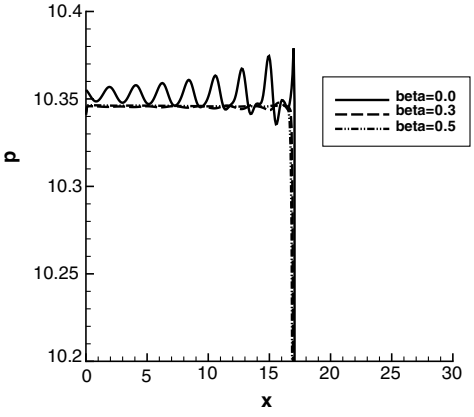

Fig. 7 Suppression of spurious oscillation in one-dimensional slowly moving shock at $t = 20$ (10,000 steps) with $\beta = 0$, 0.3 and 0.5 shows growing numerical dissipation with increased β.

V. Numerical Examples for Flows at Medium Mach Number

In this section, the ETAU scheme is tested in three typical examples with medium Mach numbers. All are compared to the exact solutions. For all the cases, $\beta = 0$ is chosen (the basic scheme). It is found there is practically no difference between the results with $\beta = 0$ and $\beta = 0.001$ because no pathological behavior occurs. In the presence of a shock, the van Albada index $\alpha = 2.0$; otherwise, $\alpha = 0.5$.

A. One-Dimensional Riemann Problem

As a one-dimensional example, the Sod shock-tube problem [25] is considered. For $x \in [0, 8]$, initially, the two flow states are separated at $x = 3$:

$$(\rho, u, p) = \begin{cases} (1, 0, 1), & \text{if } x \le 3 \\ (0.125, 0, 0.1) & \text{if } x > 3 \end{cases}$$

The physical boundary conditions at the left and right ghost cell centers, $x = -0.01$ and $x = 8.01$, are constant and, respectively, set at

$$\mathbf{V}_L = (1, 0, 1)^T \quad \text{and} \quad \mathbf{V}_R = (0.125, 0, 0.1)^T$$

There are 400 uniform cells in [0, 8]. The ETAU scheme is employed with time step size $\Delta t = 0.004$. Figures 8a and 8b show, respectively, comparisons of computed and exact results before (at $t = 2.0$) and after (at $t = 3.2$) the rarefaction and the shock exit the boundary points $x = 0$ and $x = 8$. The shock and the rarefaction are all well captured.

B. Shock Reflection on a Solid Wall

Consider a rectangular domain with $0 \le x \le 400$ and $0 \le y \le 100$, as shown in Fig. 9. A uniform triangulated grid of 40,000 cells is employed. A supersonic flow with a Mach number of 2.9 is given as the inflow boundary condition

$$u_0 = 2.9, \qquad v_0 = 0, \qquad p_0 = 1/1.4, \qquad \rho_0 = 1$$

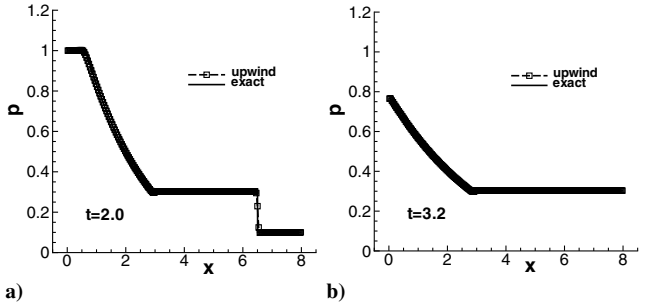

Fig. 8 One-dimensional Sod shock-tube problem; comparison of exact and numerical solutions of pressure: a) at $t = 2.0$ and b) at $t = 3.2$.

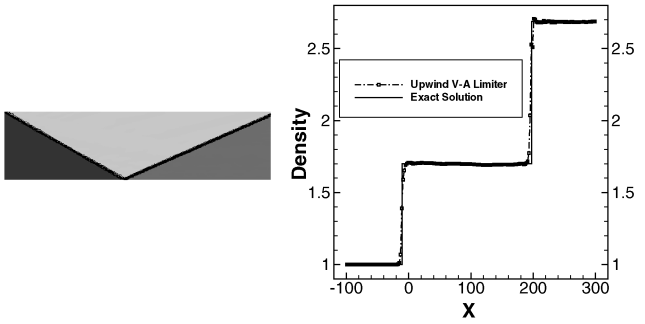

Fig. 9 Shock reflection problem: density contours (left) and comparison to the exact solution along the centerline (right).

The boundary condition at the top is an inclined flow:

$$u_{\text{top}} = 2.6193, \quad v_{\text{top}} = -0.50632, \quad p_{\text{top}} = 1.5282, \quad \rho_{\text{top}} = 1.7000$$

The outflow boundary condition is the simple extrapolation and the bottom is a solid reflecting wall. Then, a steady oblique shock is formed with 29 deg inclination and reflected at the bottom wall. Figure 9 displays the density contours and a comparison of the computed density and the exact solution along the centerline $y = 50$. Here, a van Albada limiter with $\alpha = 2$ and $\beta = 0$ (no dissipation model) is employed.

C. Propagation of Linear Acoustic Pulse and Vortex and Entropy Waves

Despite the capability of the present ETAU scheme in capturing discontinuities in flows of supersonic or hypersonic speed without suffering from the pathological behaviors, it is interesting to check its performance for flows at lower Mach number with delicate acoustic waves. Here is an example illustrating the propagation of three basic types of weak, linear waves in a two-dimensional domain [26]: namely, the linear acoustic pulse, vorticity, and entropy waves. The computational domain in the x-y plane is a square with $-100 \le x \le 100$ and $-100 \le y \le 100$. A grid with 40,000 uniform triangulated cells is used. Initially, a Gaussian acoustic pulse is located at the center of the domain (0,0) and a weaker entropy and vorticity disturbance is located off the center at (67,0):

$$p = \frac{1}{\gamma} + \delta_0 e^{-\delta_1 (x^2 + y^2)}$$

$$\rho = 1 + \delta_0 e^{-\delta_1 (x^2 + y^2)} + 0.1\delta_0 e^{-\delta_2 [(x-67)^2 + y^2]}$$

$$u = M + 0.04\delta_0 y e^{-\delta_2 [(x-67)^2 + y^2]}$$

$$v = -0.04\delta_0 (x - 67) e^{-\delta_2 [(x-67)^2 + y^2]}$$

where $\gamma = 1.4$, $\delta_1 = \ln 2/9$, and $\delta_2 = \ln 2/25$. With a small amplitude factor $\delta_0 = 0.001$, the Euler equations are practically linearized. At all four boundaries, flow variables are the given $M = 0.5$ mean flow conditions

$$p = \frac{1}{\gamma}, \qquad \rho = 1, \qquad u = M = 0.5, \qquad v = 0$$

Figure 10 shows the density contours at time $t = 63$ and its comparison to the exact solution along the x axis at $t = 63$. It is observed that the numerical solution agrees well with the exact solution. For this short-term running, $\alpha = 0.5$ and $\beta = 0$ are chosen. The example shows the performance of the ETAU scheme with weak, delicate acoustic waves.

VI. Numerical Examples for Flows at Low Mach Number

To test the ETAU scheme with flows at low Mach numbers, we consider flow past a circular cylinder (or cylinders). As the Reynolds numbers are high, vortex roll up occurs in the wake and von Karman vortex streets are formed. The flows are highly unsteady and

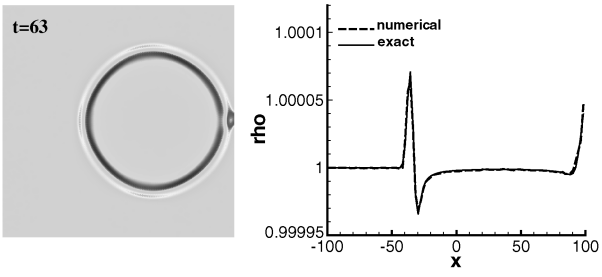

Fig. 10 Propagation of linear waves: instantaneous density contours at time $t = 63$ (left) and comparison between exact and numerical solutions along the centerline $y = 0$ at $t = 63$ (right).

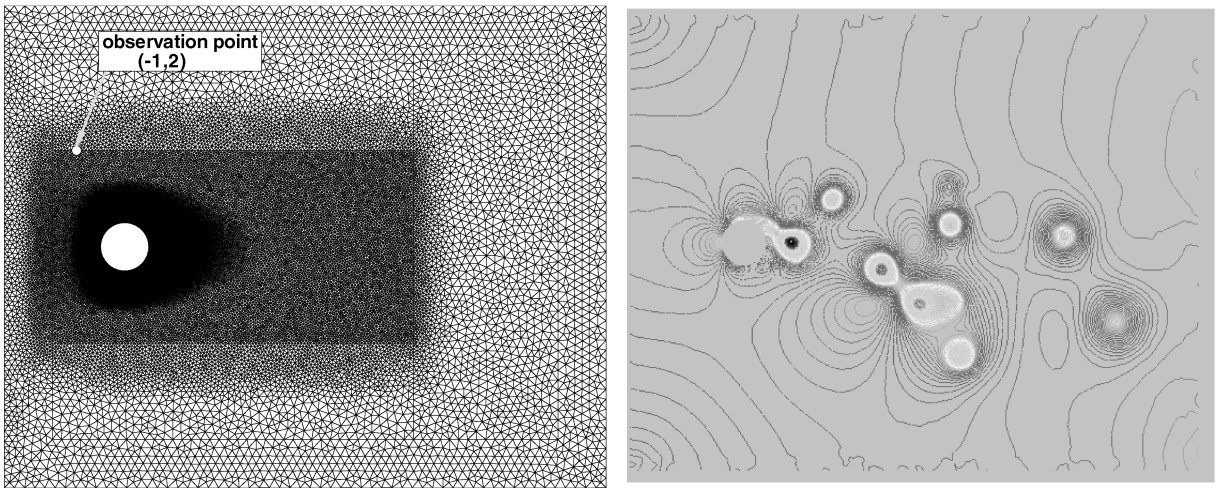

Fig. 11 $M = 0.2$ flow past a circular cylinder: the computational domain with unstructured grid, showing the location of the observation point (left) and snapshot of isobars at time step 250,000 (right).

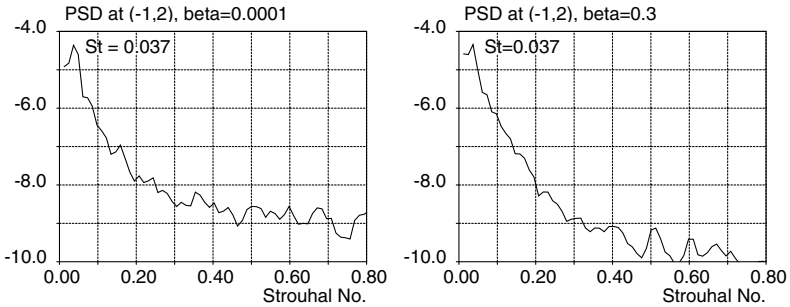

Fig. 12 PSD at a field point $(-1, 2)$ with different βs: $\beta = 0.0001$ (left) and $\beta = 0.3$ (right), showing that β has no influence on the PSD and Strouhal number at the peak (PSD $= -4.36$ and $Sr = 0.037$); because of the larger β, the PSD curve on the right decays faster with increasing Strouhal number.

accompanied by aeolian noise. These examples are aeroacoustics computations, which demonstrate the time accuracy of the scheme at low Mach number and its performances for viscous flow. The three examples include a single circular cylinder or twin circular cylinders with the Mach number ranging from $M = 0.2$ to $M = 0.02$. The computed results are compared to the available experimental data. For the lowest Mach number $M = 0.02$, no preconditioning is invoked. The van Albada index is always set at $\alpha = 0.5$ and β at 0.001 except where different β are used for comparisons.

A. Flow Past a Single Circular Cylinder at $M = 0.2$ with Aeolian Noise

Aeolian noise is the noise generated by flow past a circular cylinder (or cylinders). First, consider a single circular cylinder with a diameter $D = 1.9$ cm subject to a flow with a freestream Mach number $M = 0.2$ [27]. The Reynolds number is $Re = 90,000$. The diameter D is used as the length scale. For convenience, the freestream speed of sound and density are used as scales for nondimensionalization. The Strouhal number (nondimensional frequency) is here conveniently defined based on D and the freestream speed of sound. The computational domain contains about 91,000 triangular cells, spanning between $-2.5 \le x \le 10$ and $-5 \le y \le 5$, with the center of the circular cylinder located at (0,0). Initially, the flow is quiescent:

$$(\rho_0, u_0, v_0, p_0) = (1.0, 0, 0, 1/\gamma)$$

The boundary conditions at the inflow, top and bottom, are the given $M = 0.2$ flow:

$$p = \frac{1}{\gamma}, \qquad \rho = 1, \qquad u = M = 0.2, \qquad v = 0$$

Simple extrapolation is applied to the outflow boundary and no-slip condition at the cylinder wall. With a van Albada limiter $\alpha = 0.5$ and $\beta = 0.0001$, 80,000 time steps were computed to ensure the initial startup transients have exited the domain. During the next 170,000 time steps, the pressure history at an observation point $(-1, 2)$ in the field are recorded. The point is located outside the vortex streets to ensure that only acoustic wave fluctuations are recorded. Figure 11 shows the grid and the instantaneous isobars at this final time step. Vortex streets downstream of the cylinder are clearly observed. Then, fast Fourier transform (FFT) analysis is applied to the pressure history. The results are presented as a PSD (power spectral density) plot in Fig. 12. There are 17,000 sampling points (recorded every 10 time steps) in the pressure history file, which is just enough to cover $2^{14} = 16,384$ points for FFT. In Fig. 12, the single peak of PSD corresponds to a Strouhal number $St = 0.037$, which compares very well with the experimental data [27] (Table 1). Note that this St is

Table 1 Comparison of experimental and computed aeolian noise frequencies.

Mach number	Reynolds number	Number of cylinders	Exp. freq. (Strouhal number)	Comput. freq. (Strouhal number)	CPU time, h
0.2	90,000	Single	0.1846 [27]	0.185	8.57
0.0714	15,800	Twin	0.205 [28]	0.21	27.88
0.02	15,000	Single	0.195 [29]	0.195	195.4

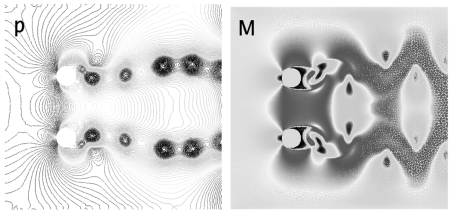

Fig. 13 Snapshot of isobars (left) and snapshot of iso-Mach numbers (right) at time step 740,000 for the twin cylinder aeolian noise problem with a freestream $M = 0.0714$, $\beta = 0.001$, showing vortex streets, as well as the grid; the buffer zone is not shown.

converted to 0.185 in Table 1 based on the freestream velocity, as will be explained at the end of this section. Figure 12 also shows that the value of β has little influence on the Strouhal numbers at the curve peaks. However, the larger value of β (e.g., 0.3) represents larger dissipation: the corresponding PSD curve is smoother and decays faster for $St \geq 0.2$.

B. Flow Past Twin Circular Cylinders at $M = 0.0714$

Similar computations are conducted for the aeolian noise problem with twin cylinders. The diameter of the cylinders is $D = 0.955$ cm and the cylinders are placed vertically $3D$ apart (see Fig. 13) and subjected to a freestream with a Mach number $M = 0.0714$ [28]. The computational domain is about the same dimensions as the single cylinder case, with a small buffer zone at the downstream outflow boundary. There are about 100,000 triangular cells in the domain. All the boundary conditions are the same as in the previous case except $M = 0.0714$. At a designated point $(-1, 2)$, the pressure history is recorded after 80,000 steps at every 20 steps for 660,000 additional time steps. There are 33,000 sample points in the pressure history file, which slightly exceeds $2^{15} = 32,768$ for FFT. Figure 13 shows the instantaneous isobars and iso-Mach numbers at time step 740,000 and the interaction between the two vortex streets from the twin cylinders. The computed Strouhal number is presented in Table 1 and agrees well with the experimental one.

C. Flow Past Circular Cylinder at a Low $M = 0.02$

In the preceding example, the computational domain, the grid, and the boundary conditions are identical to the previous case with single cylinder, except the Mach number M is reduced to 0.02 and the Reynolds number is set at 15,000. The same parameters $\alpha = 0.5$, $\beta = 0.001$, and $\Delta t = 0.002$ are used. However, as the flow is now much slower, it takes more than 1.5 million time steps to allow the initial startup transient flow to pass through the domain. A pressure history at three locations are recorded over 4.1 million additional time steps. To ensure numerical accuracy over a long run time, the computation is carried out in double-precision mode. Figure 14 illustrates snapshots of the vortex streets in the wake of the circular

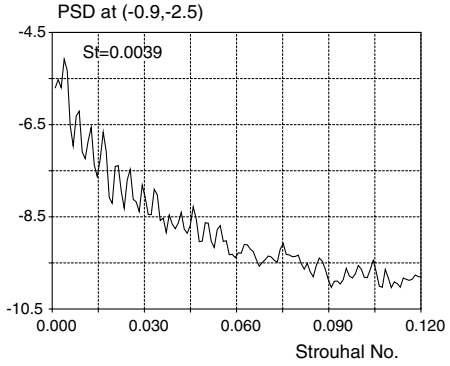

Fig. 15 PSD at a field point $(-0.9, -2.5)$, showing a Strouhal number $Sr = 0.0039$, which agrees with the experimental data in [29].

cylinder flow at time steps 2.3 million and 5.7 million. FFT analysis is again applied to the pressure history. The result is presented as a PSD plot in Fig. 15. There are 16,400 sampling points (recorded every 250 time steps) in the pressure history file.

We note that for all three test cases, the Strouhal number based on the freestream speed of sound is used, which is convenient in numerical computations. In Table 1, for comparison, it is converted back to the standard Strouhal number, which is based on the freestream flow velocity. Table 1 demonstrates that for either $M = 0.2$, 0.0714, or 0.02, the computed frequencies (Strouhal numbers) agree well with the experimental data [27–29]. These computations were run on a Linux workstation with 2 GHz CPU. The CPU times are also listed in the table. To obtain a time series of adequate size for FFT, the required CPU time increases quickly with the reduction of the Mach number.

VII. Conclusions

As a result of striking a balance between accuracy, efficiency, and affordable computer resources (CPU time and memory), an ETAU finite volume method for unsteady Euler and Navier–Stokes equations is presented. The ETAU scheme is nominally second-order-accurate in space and time. The scheme adopts concepts from high-order upwind schemes, such as the Cauchy–Kowalewski time stepping, accurate evaluation of surface fluxes, multidimensional limiter, etc. Also, employment of the unstructured grid enables flexibility in geometry.

A built-in multidimensional dissipation model in the ETAU scheme helps to suppress the pathological behaviors and stabilize the computation for high-Mach-number flows. The parameter β in the model is associated with the amount of artificial dissipation imposed. Generally, $\beta = 0.001$ is good enough for most flows. However, for flows with high Mach number, strong shocks, and associated

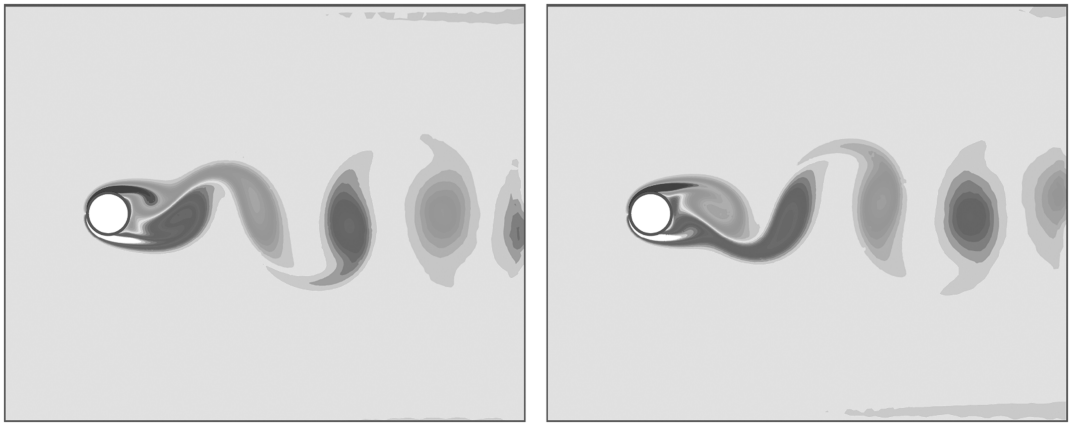

Fig. 14 $M = 0.02$ flow past a circular cylinder: snapshot of vortex streets at time step 2.3 million (left) and snapshot of vortex streets at time step 5.7 million (right).

pathological behaviors, β may need to increase to the level of 10^{-1}. To avoid excessive dissipation, β should be kept as small as possible.

The van Albada index α is associated with the multidimensional limiter. If the multidimensional minmod limiter is used, no additional parameters are required. For flows at high Mach numbers with shocks, α is usually set at 2.0, otherwise, α should be smaller.

In addition, the ETAU scheme also exhibits good performance as an all-speed or Mach-number-insensitive scheme. As demonstrated in the examples, for Mach number from $M = 0.02$ to 10, the scheme works well, one needs only to adjust one or two parameters: namely, β and α. No preconditioning is invoked at low Mach numbers.

To conclude, the ETAU scheme is a stabilized upwind scheme of almost all speed. It is time accurate and works well with viscous or inviscid flows that are associated with either strong shocks or with delicate acoustic waves. Employment of unstructured grid provides not only flexibility in geometry but also balanced loading for large-scale parallel computation. The ETAU scheme is rendered as a robust and viable tool for practical CFD and CAA computations.

Acknowledgments

This work received support from the Supersonics Project Office of NASA John H. Glenn Research Center at Lewis Field. The authors are thankful to H. T. Huynh for providing the two-dimensional Roe approximate Riemann solver.

References

[1] Huynh, H. T., "Analysis and Improvement of Upwind and Centered Schemes on Quadrilateral and Triangular Mesh," AIAA Paper 2003-3541, 2003.

[2] Nessyahu, H., and Tadmor, E., "Non-Oscillatory Central Differencing for Hyperbolic Conservation Laws," *Journal of Computational Physics*, Vol. 87, No. 2, 1990, pp. 408–463. doi:10.1016/0021-9991(90)90260-8

[3] Chang, S.-C., Wang, X.-Y., and Chow, C.-Y., "The Space-Time Conservation Element and Solution Element Method—A New High-Resolution and Genuinely Multidimensional Paradigm for Solving Conservation Laws," *Journal of Computational Physics*, Vol. 156, No. 1, 1999, pp. 89–136. doi:10.1006/jcph.1999.6354

[4] Wang, X.-Y., and Chang, S.-C., "A 2-D Non-Splitting Unstructured Triangular Mesh Euler Solver Based on the Space-Time Conservation Element and Solution Element Method," *Computational Fluid Dynamics Journal*, Vol. 8, No. 2, 1999, pp. 309–325.

[5] Godunov, S. K., "A Finite Difference Method for the Numerical Computation of Discontinuous Solutions of the Equations of Fluid Dynamics," *Matematicheski Sbornik*, Vol. 47, 1959, pp. 357–393.

[6] van Leer, B., "Towards the Ultimate Conservative Scheme. 4. A New Approach to Numerical Convection," *Journal of Computational Physics*, Vol. 23, No. 3, 1977, pp. 276–298. doi:10.1016/0021-9991(77)90095-X

[7] Shu, C.-W., and Osher, S., "Efficient Implementation of Essentially Non-Oscillatory Shock-Capturing Schemes, 2," *Journal of Computational Physics*, Vol. 83, No. 1, 1989, pp. 32–78. doi:10.1016/0021-9991(89)90222-2

[8] Jiang, G.-S., and Shu, C.-W., "Efficient Implementation of ENO Schemes," *Journal of Computational Physics*, Vol. 126, No. 1, 1996, pp. 202–228. doi:10.1006/jcph.1996.0130

[9] Cocksburn, B., and Shu, C.-W., "The Runge–Kutta Discontinuous Galerkin Method for Conservation Laws 5: Multidimensional Systems," *Journal of Computational Physics*, Vol. 141, No. 2, 1998, pp. 199–224. doi:10.1006/jcph.1998.5892

[10] Wang, Z. J., and Liu, Y., "Spectral (Finite) Volume Method for Conservation Laws on Unstructured Grids 4: Extension to Two-Dimensional Systems," *Journal of Computational Physics*, Vol. 194, No. 2, 2004, pp. 716–741. doi:10.1016/j.jcp.2003.09.012

[11] Liu, Y., Vinokur, M., and Wang, Z. J., "Spectral Difference Method for Unstructured Grids 1: Basic Formulation," *Journal of Computational Physics*, Vol. 216, No. 2, 2006, pp. 780–801. doi:10.1016/j.jcp.2006.01.024

[12] Loh, C. Y., and Jorgenson, P. C. E., "A Time-Accurate Upwind Unstructured Finite Volume Method for Compressible Flow with Cure of Pathological Behaviors," AIAA Paper 2007-4463, 2007.

[13] Quirk, J. J., "A Contribution to the Great Riemann Solver Debate," *International Journal for Numerical Methods in Fluids*, Vol. 18, No. 6, 1994, pp. 555–574. doi:10.1002/fld.1650180603

[14] Gressier, J., and Moschetta, J.-M., "On the Pathological Behavior of Upwind Schemes," AIAA Paper 98-0110, 1998.

[15] Lin, H.-C., " Dissipation Additions to Flux-Difference Splitting," *Journal of Computational Physics*, Vol. 117, No. 1, 1995, pp. 20–27. doi:10.1006/jcph.1995.1040

[16] Xu, K., and Li, Z., "Dissipative Mechanism in Godunov-Type Schemes," *International Journal for Numerical Methods in Fluids*, Vol. 37, No. 1, 2001, pp. 1–22. doi:10.1002/fld.160

[17] Xu, K., "A Gas-Kinetic BGK Scheme for the Navier–Stokes Equations and Its Connection with Artificial Dissipation and Godunov Method," *Journal of Computational Physics*, Vol. 171, No. 1, 2001, pp. 289–335. doi:10.1006/jcph.2001.6790

[18] Loh, C. Y., and Jorgenson, P. C. E., " Multi-Dimensional Dissipation for Cure of Pathological Behaviors of Upwind Scheme," *Journal of Computational Physics*, Vol. 228, No. 5, 2009, pp. 1343–1346. doi:10.1016/j.jcp.2008.10.044

[19] Kitamura, K., Roe, P., and Ismail, F., "Evaluation of Euler Fluxes for Hypersonic Flow Computations," *AIAA Journal*, Vol. 47, No. 1, 2009, pp. 44–53. doi:10.2514/1.33735

[20] Hirsch, C., *Numerical Computation of Internal and External Flows*, Vols. 1–2, Wiley, New York, 1993.

[21] Delanaye, M., and Liu, Y., "Quadratic Reconstruction Finite Volume Schemes on 3D Arbitrary Unstructured Polyhedral Grids," AIAA Paper 99-3259, 1999.

[22] Roe, P. L., "Approximate Riemann Solvers, Parameter Vectors, and Difference Schemes," *Journal of Computational Physics*, Vol. 43, No. 2, 1981, pp. 357–372. doi:10.1016/0021-9991(81)90128-5

[23] van Albada, G. D., van Leer, B., and Roberts, W. W. Jr., "A Comparative Study of Computational Methods in Cosmic Gas Dynamics," *Astronomy and Astrophysics*, Vol. 108, No. 1, 1982, pp. 76–84.

[24] Gnoffo, P., "Simulation of Stagnation Region Heating in Hypersonic Flow on Tetrahedral Grids," AIAA Paper 2007-3960, 2007.

[25] Sod, G. A., "A Survey of Several Finite Difference Methods for Systems of Nonlinear Hyperbolic Conservation Laws," *Journal of Computational Physics*, Vol. 27, No. 1, 1978, pp. 1–31. doi:10.1016/0021-9991(78)90023-2

[26] Hardin, J. C., Ristorcelli, J. R., and Tam, C. K. W. (eds.), *ICASE/LaRC Workshop on Benchmark Problems in Computational Aeroacoustics (CAA)*, CP-3300, NASA, May 1995.

[27] Hardin, J. C., "Solution Comparisons: Category 4," *2nd Computational Aeroacoustics (CAA) Workshop on Benchmark Problems*, edited by C. K. W. Tam, and J. C. Hardin, NASA CP-3352, June 1997, pp. 373–375.

[28] Dahl, M. (ed.), *4th Computational Aeroacoustics (CAA) Workshop on Benchmark Problems*, CP-2004-212954, NASA, Sept. 2004.

[29] Schlichting, H., *Boundary-Layer Theory*, McGraw–Hill, New York, 1979.

K. Anderson
Associate Editor